Supplementary information for

Investigation of the Chemical Structure of Core–Shell Fe_3O_4@$Ni_{1-x}Co_xFe_2O_4$ Nanoparticles and its Influence On Their Magnetic Properties

Raul Lopez-Martin,[a,i] Iryna Makarchuk,[b,i] , Fadi Choueikani,[c] Simon Hettler,[d,e,f] Raul Arenal,[e,f,g] Jose A. De Toro,[a] Benoit P. Pichon [b,h,*]

[a] Instituto Regional de Investigación Científica Aplicada (IRICA) and Departamento de Física Aplicada, Universidad de Castilla-La Mancha, 13071 Ciudad Real, Spain
[b] Université de Strasbourg, CNRS, Institut de Physique et Chimie des Matériaux de Strasbourg, UMR 7504, F-67000 Strasbourg, France
[c] Synchrotron SOLEIL, L'Orme des Merisiers, Departementale 128, 91190 Saint-Aubin, France
[d] Laboratoty for Electron Microscopy (LEM), Karlsruhe Institute for Technology, Engesserstr. 7, 76131 Karlsruhe, Germany
[e] Instituto de Nanociencia y Materiales de Aragon (INMA), CSIC-Universidad de Zaragoza, Calle Pedro Cerbuna 12, 50009 Zaragoza, Spain
[f] Laboratorio de Microscopías Avanzadas (LMA), Universidad de Zaragoza, Calle Mariano Esquillor, 50018 Zaragoza, Spain
[g] ARAID Foundation, 50018 Zaragoza, Spain
[h] Institut Universitaire de France, 75231 CEDEX 05 Paris, France
[i] These authors have contributed equally to this work.

Corresponding author
benoit.pichon@ipcms.unistra.fr

Synthesis of metal precursors

Iron (II) stearate ($FeSt_2$) was synthesized following a protocol that was already published for the iron stearate.[43] In a 1 L two-necked round-bottom flask, 9.8 g (32 mmol) of sodium stearate (98.8%, TCI) were poured and 320 mL of distilled water were added. The mixture was heated to reflux under magnetic stirring until all the stearate was dissolved. Afterward, 3.80 g (16 mmol) of iron (II) chloride tetrahydrate was dissolved in 160 mL of distilled water and was poured into a round-bottom flask. The mixture was heated to reflux and kept at this temperature for 15 min under magnetic stirring before cooling down to room temperature. The colored precipitate was collected by centrifugation (15 000 rpm, 5 min) and washed by filtration with a Buchner funnel. Finally, the powder was dried in an oven at 65 °C for 15 h.

Cobalt (II) stearate ($CoSt_2$) was synthesized following a protocol that was already published.[44] In a 1 L two-necked round-bottom flask, 9.8 g (32 mmol) of sodium stearate (98.8%, TCI) were poured and 320 mL of distilled water were added. The mixture was heated to reflux under magnetic stirring until all the stearate was dissolved. Afterward, 3.16 g (16 mmol) of cobalt (II) chloride hexahydrate was dissolved in 160 mL of distilled water and was poured into a round-bottom flask. The mixture was heated to reflux and kept at this temperature for 15 min under magnetic stirring before cooling down to room temperature. The colored precipitate was collected by centrifugation (15 000 rpm, 5 min) and washed by filtration with a Buchner funnel. Finally, the powder was dried in an oven at 65 °C for 15 h.

Nickel (II) octanoate ($NiOct_2$) was synthesized following a protocol that was synthesized following a modified protocol for the cobalt (II) stearate synthesis. In a 1 L two-necked round-bottom flask, 5.3 g (32 mmol) of sodium octanoate were poured and 320 mL of distilled water were added. The mixture was heated to reflux under magnetic stirring until all the stearate was dissolved. Afterward, 3.8 g (16 mmol) of nickel (II) chloride hexahydrate was dissolved in 160 mL of distilled water and was poured into a round-bottom flask. The mixture was heated to reflux and kept at this temperature for 15 min under magnetic stirring before cooling down to room temperature. The colored precipitate was collected by centrifugation (15 000 rpm, 5 min) and washed by filtration with a Buchner funnel. Finally, the powder was dried in an oven at 65 °C for 15 h.

Cobalt (II)xNickel (II) mixed stearate ($CoSt_2xNiSt_2$) was synthesized following a modified protocol for the cobalt (II) stearate synthesis. In a 1 L two-necked round-bottom flask, 9.8 g (32 mmol) of sodium stearate (98.8%, TCI) were poured and 320 mL of distilled water were added. The mixture was heated to reflux under magnetic stirring until all the stearate was dissolved. Afterward, 1.9 g (8 mmol) of cobalt (II) chloride hexahydrate and 1.9 g (8 mmol) of nickel (II) chloride hexahydrate was dissolved in 160 mL of distilled water and was poured into a round-bottom flask. The mixture was heated to reflux and kept at this temperature for 15 min under magnetic stirring before cooling down to room temperature. The colored precipitate was collected by centrifugation (15 000 rpm, 5 min) and washed by filtration with a Buchner funnel. Finally, the powder was dried in an oven at 65 °C for 15 h.

Study of the thermal stability of metal complexes

In order to synthesize nanoparticles with narrow size distibution and well-defined shape, the precise control of the thermal decomposition of metal complexes is mandatory. The chemical composition of metal complexes and the strength of the interaction between the metal and the ligands were studied by Fourier transformed infrared (FTIR) spectroscopy. Thermal gravimetry (TG) analysis was also performed for each metal complex in order to study their thermal stability.

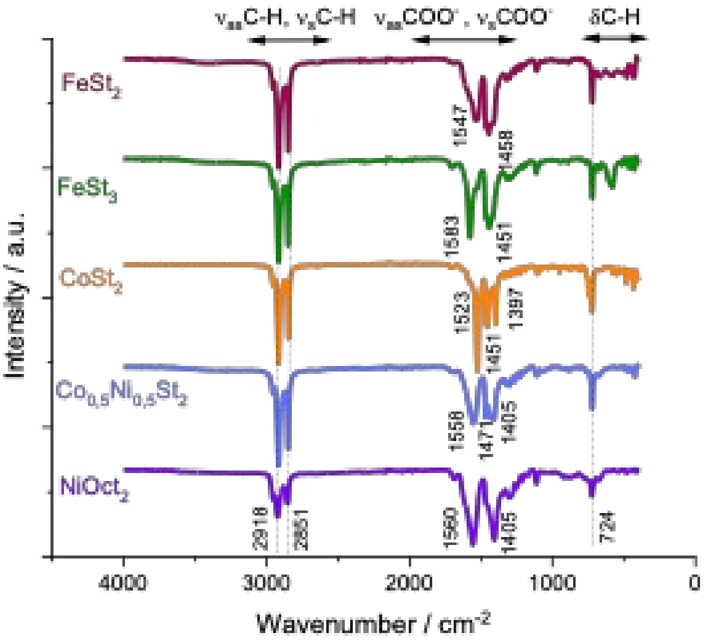

Figure S1. FTIR spectra of the metal precursors used for the synthesis of the core-shell nanoparticles by thermal decomposition.

The FTIR spectra show bands which are typical of metal stearate complexes (Figure S1). Bands at 2918 and 2851 cm^{-1} correspond to asymmetric (ν_{as}C-H) and symmetric (ν_sC-H) stretching vibration modes of C-H bonds in alkylene chains. The bands at 724 cm^{-1} are characteristic of the scissoring mode of δH-C-H of alkylene chains. Bands at 1560 cm^{-1} and 1450 cm^{-1} are ascribed to asymmetric (ν_{as}C-O) and symmetric (ν_sC-O) stretching vibration modes of C-O bonds in carboxylic acid groups which interact with a metal. The contribution around 1700 cm^{-1} is very weak, which agree with few amounts of free carboxylic acid groups, i.e., alkynoate molecules interacting with metals. The difference Δ between ν_{as}C-O and ν_sC-O depends on the coordination mode of the ligand with the metal.[67] The calculated values correspond to chelating mode $\Delta < 100$ cm^{-1}) for CoSt$_2$, NiOct$_2$, Fe$_{0.5}$Ni$_{0.5}$St$_2$ complexes and bridging bidentate ($140 < \Delta < 190$ cm^{-1}) for FeSt$_3$ and FeSt$_2$ complexes.

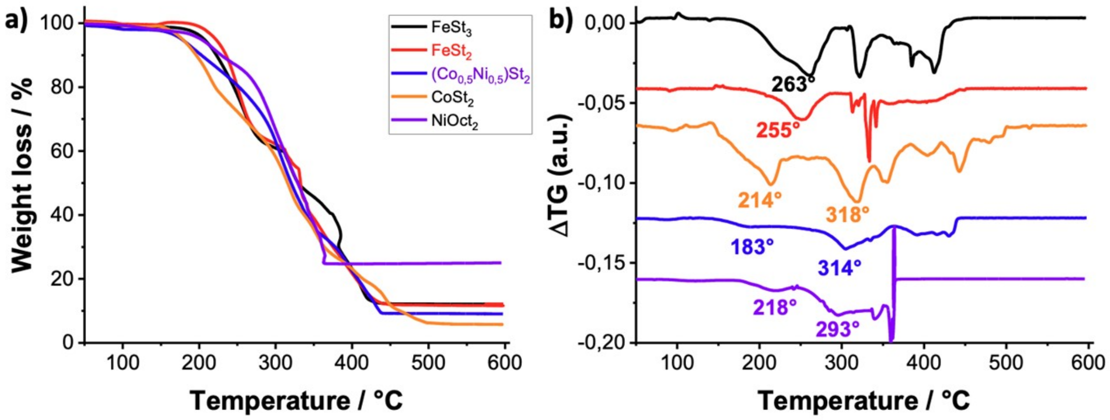

Figure S2. Thermal gravimetric (TG) curves of the metal complexes used for the synthesis of the core-shell nanoparticles by thermal decomposition. a) Weight loss as a function of temperature and, b) the corresponding derivatives.

The thermal stability of metal complexes was investigated by TG analysis under air (Figure S2a). Weight losses are observed for all metal complexes at temperatures from 200 °C up to 450 °C (350 °C for $NiOct_2$ and 500 °C for $CoSt_2$). The weight loss is not constant and consists in different steps of the decomposition of metal complexes. Derivatives of the corresponding TG curves (Figure S2b) give a better insight on the decomposition mechanism which can be considered as a nucleation / growth process of metal oxide formation. [68,69] No peak is observed at 100 °C, indicating the absence of free water molecules. The first broad contributions (180 - 270 °C) are usually attributed to the decomposition of the metal complex (nucleation) which is followed by the formation of the metal oxides (growth) around (290 - 320 °C).

$CoSt_2$ decomposes at a lower temperature (214 °C) than $FeSt_2$ (255 °C) and $FeSt_3$ (263 °C) which agree with lower thermal stability. $NiOct_2$ presents a similar thermal stability (218 °C), even though it has a shorter allylene chain. The mixed complex $Fe_{0.5}Ni_{0.5}St_2$ is less stable than the rest and decomposes at 183 °C. Although it is very complex to establish the relationship between the structure of these metal complexes and their thermal stability, it can be related to the position of the νC-O bands since the Δ values reflect the coordination mode (Figure S1). The comparison of Differential Thermogravimetric analysis (DTG) curves and FTIR spectra show that the bridging bidentate mode in $CoSt_2$, $NiOct_2$, $Fe_{0.5}Ni_{0.5}St_2$ favors a better thermal stability than the chelating mode in $FeSt_3$ and $FeSt_2$ complexes.[67] These are important information to set the experimental conditions such as the solvent with specific boiling temperature as well as to study the mechanism formation of such complex structures.

The formation of the metal oxide does not follows the same trend observe for the decomposition of metal complexes. Nickel oxide forms at a much lower temperature (293°C) than the other oxides (around 318°C).

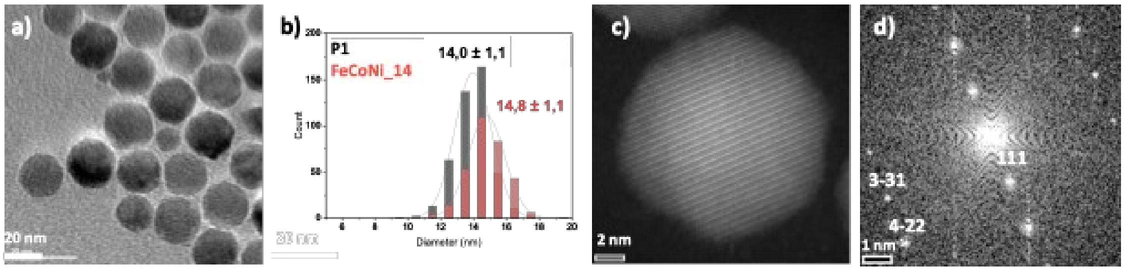

Figure S3. FeCoNi_14 nanoparticles. a) TEM micrograph and b) the corresponding size distribution which is compared to that of the pristine iron oxide nanoparticles. c) HRSTEM micrograph and d) the FFT calculated for the main NP. The measured reflections are attributed to the spinel phase.

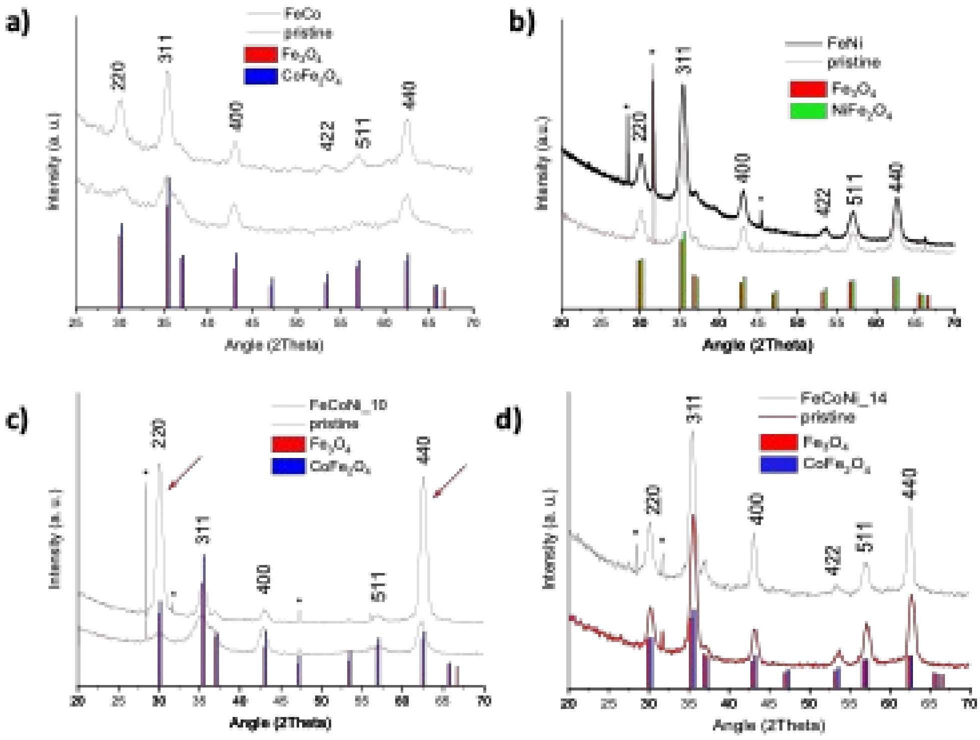

Figure S4. XRD patterns of core-shell nanoparticles and the corresponding pristine nanoparticles.

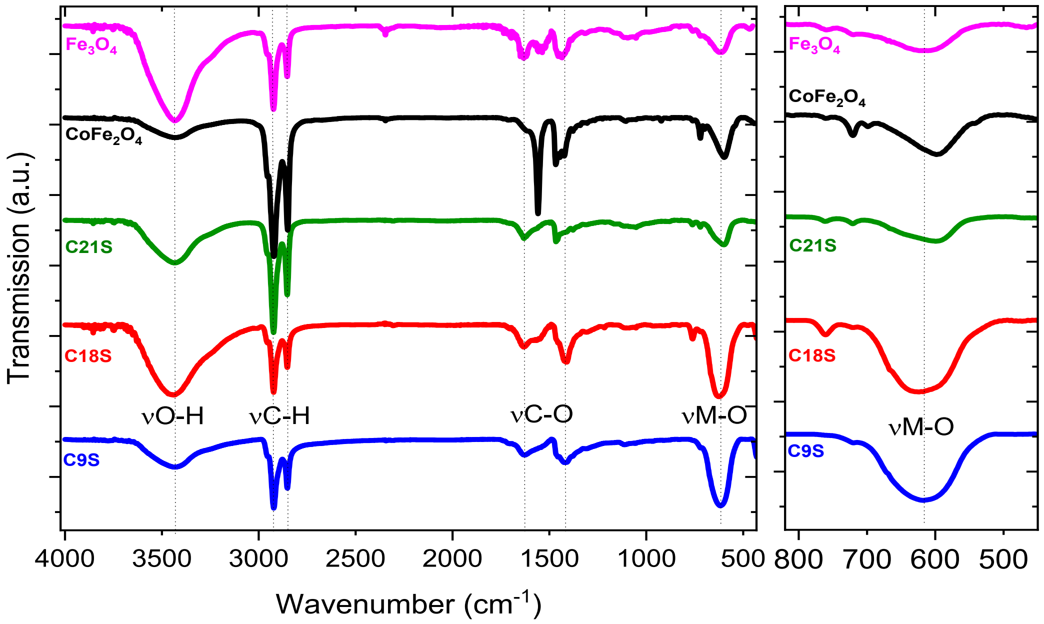

Figure S5. FTIR spectra of the FeCo, FeNi, FeCoNi_10 core-shell nanoparticles.

FTIR spectra show typical absorption bands of transition metal oxide nanoparticle coated with oleic acid molecules. Stretching bands of hydroxide (ν_{O-H}), hydrocarbon chains (ν_{C-H}) and carboxylic acid (ν_{C-O}) groups are ascribed to oleic acid molecules. A broad band centered at 700-600 cm^{-1} is ascribed to transition metal oxides (ν_{M-O}) and shifts from 600 cm^{-1} to higher wavelengths with increase of the Ni/Co atomic ratio.

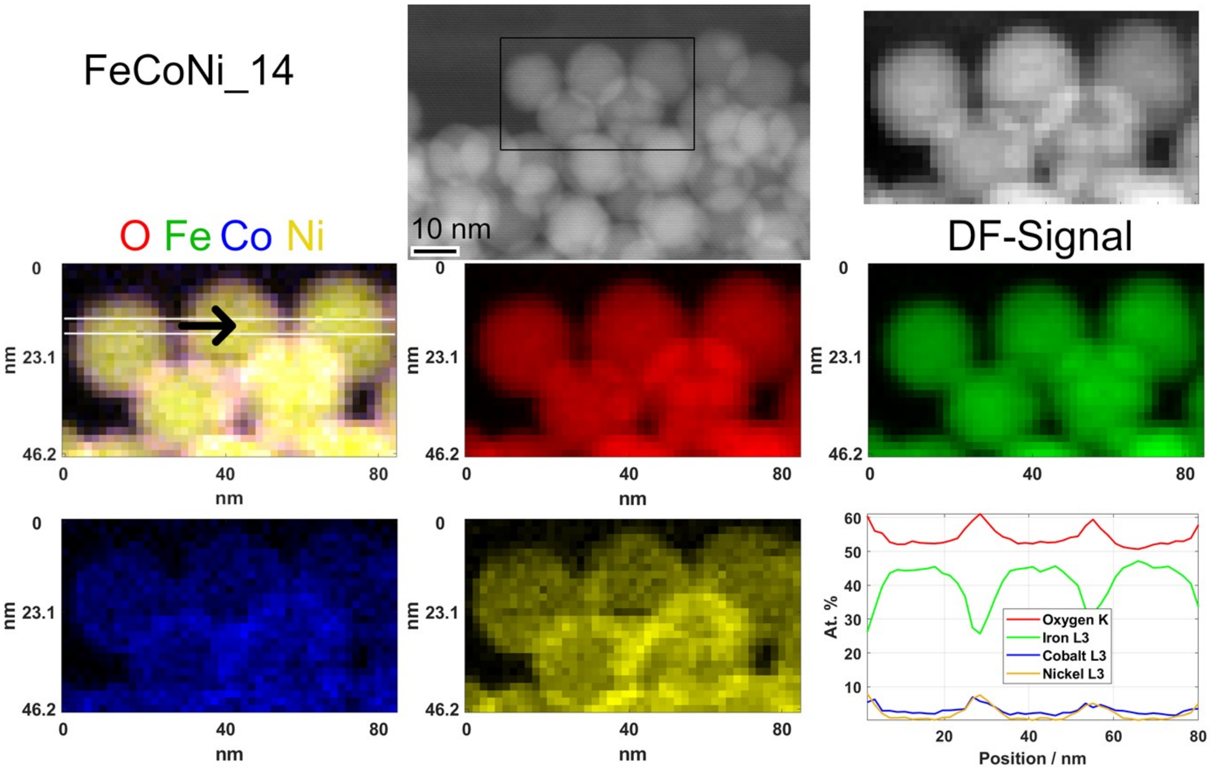

Figure S6. EELS SI analysis of FeCoNi_14 nanoparticles. a) Survey DF image with rectangle corresponding to the analyzed region. b) DF image acquired during the EELS analysis. c) Composite chemical map and the corresponding d-g) element specific maps with oxygen (red), iron (green), cobalt (blue) and nickel (yellow). h) Line profile as marked in c) corresponding to the upper three nanoparticles. The chemical map suggests the coverage of the iron oxide pristine nanoparticles with a homogeneous spatial distribution of cobalt and nickel mixture, corresponding to a core-shell structure.

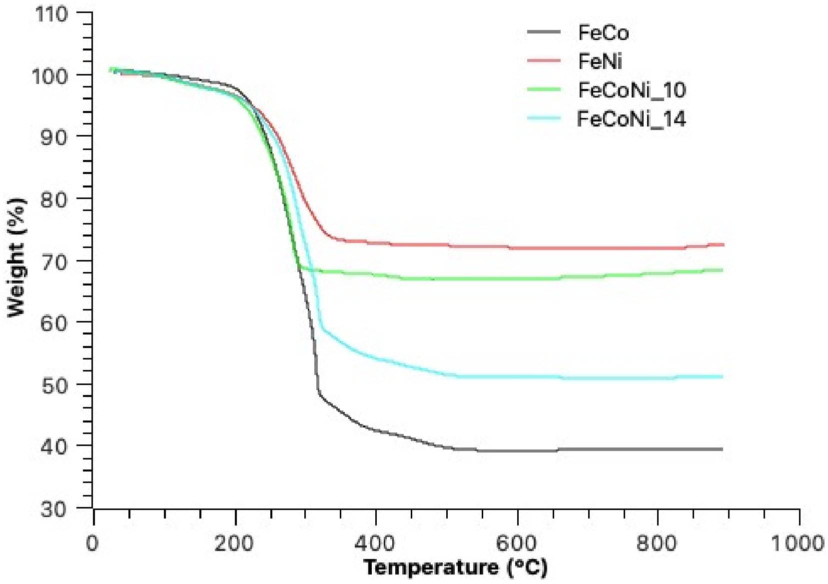

Figure S7. Thermogravimetric analysis of the core-shell nanoparticles.

The weight loss corresponds to the decomposition of oleic acid molecules which interact with the surface of the nanoparticles.

XAS/XMCD spectroscopy

XMCD spectra were normalized by the XAS signal in order to determine the fraction of uncompensated spins, i.e. the cation (Fe, Co and Ni) distribution between the spinel and the wüstite phases.

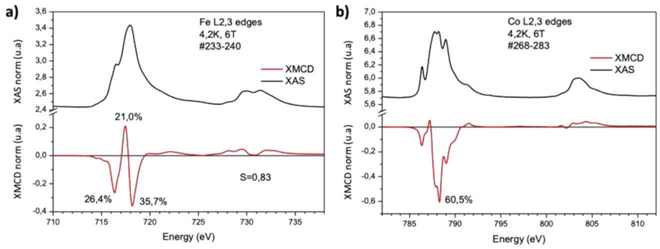

Figure S8. XAS spectra and corresponding normalized XMCD spectra for FeCo nanoparticles at a) Fe $L_{2,3}$ edge and a) Co $L_{2,3}$ edge.

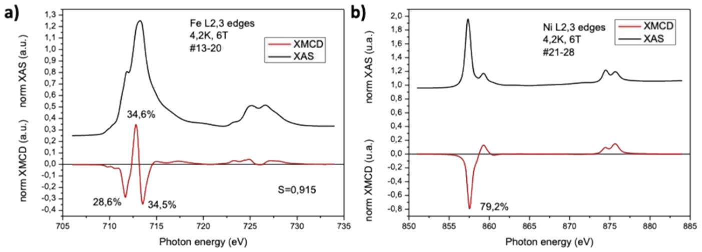

Figure S9. XAS spectra and corresponding normalized XMCD spectra for FeNi nanoparticles at a) Fe $L_{2,3}$ edge and a) Co $L_{2,3}$ edge.

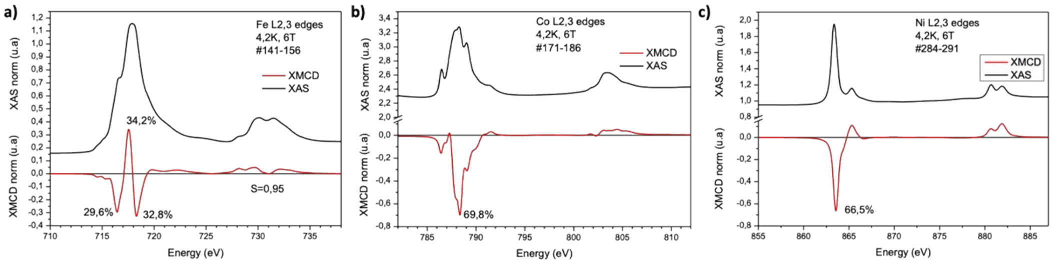

Figure S10. XAS spectra and corresponding normalized XMCD spectra for FeCoNi_10 nanoparticles at a) Fe $L_{2,3}$ edge and a) Co $L_{2,3}$ edge.

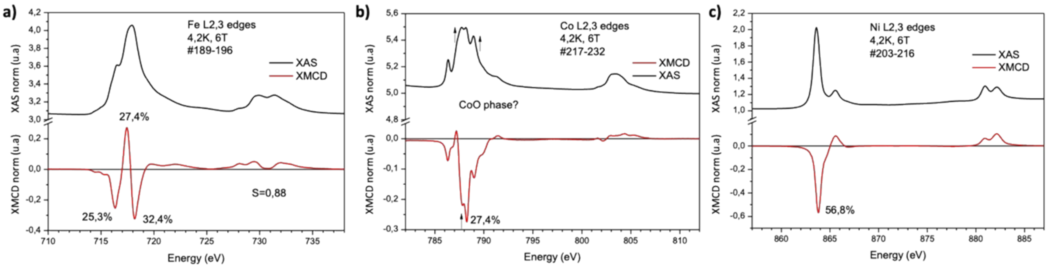

Figure S11. XAS spectra and corresponding normalized XMCD spectra for FeCoNi_14 nanoparticles at a) Fe $L_{2,3}$ edge and a) Co $L_{2,3}$ edge.

Magnetic characterization of the magnetite core

Figure S12 shows a comparison of the FC-ZFC of the samples FeCo, FeCoNi_10, FeNi and the magnetite core used for the synthesis of FeCoNi_10. Assuming that the core (of similar size) of all these samples have the same effective anisotropy, a decrease in the magnetic anisotropy is directly seen for FeNi from the position of the peak of the ZFC.

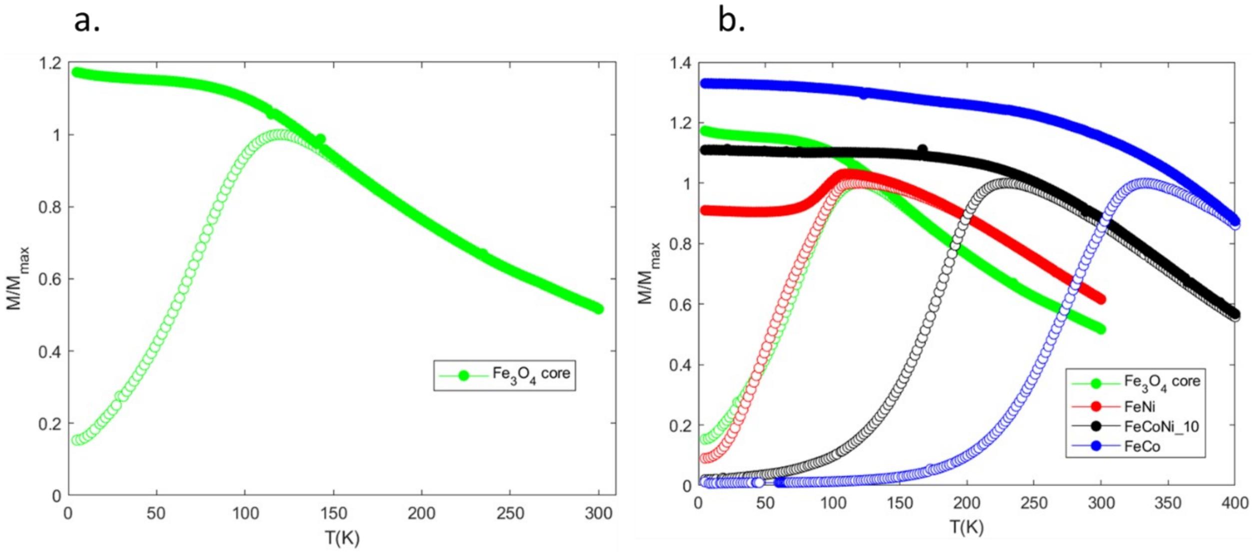

Figure S12. FC-ZFC M(T) curves. a) Pristine iron oxide nanoparticles (P1) nanoparticles. b) Comparison of the magnetite core with samples of similar size.

From the ZFC-FC curves (Figures 5a and 5b of the main text) and from Figure S12, we are able to extract the distribution of blocking temperatures in our samples (Figure S13). A low temperature peak in the magnetite core curve is seen. Together with the shifted loop after FC (Figure S14), this may indicate the existence of a freezing process of a shell of disordered spins at the surface of the magnetite core particle (P1).

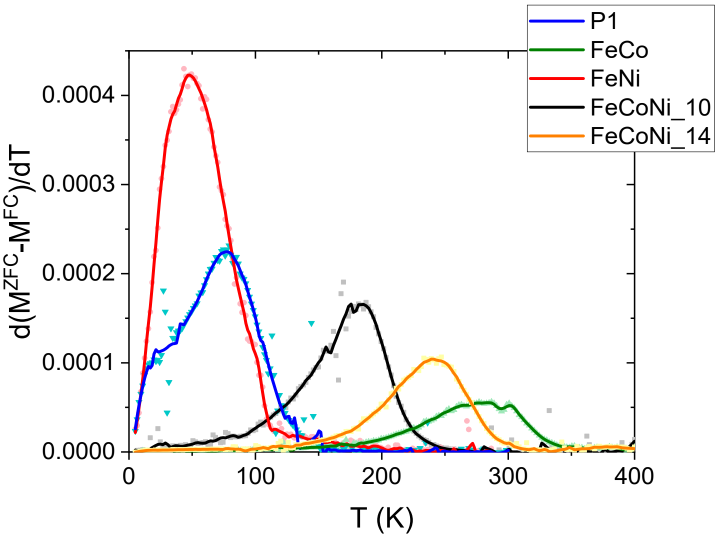

Figure S13. Distribution of blocking temperatures for all samples under study. A smoothing curve has been used as a guide to the eye.

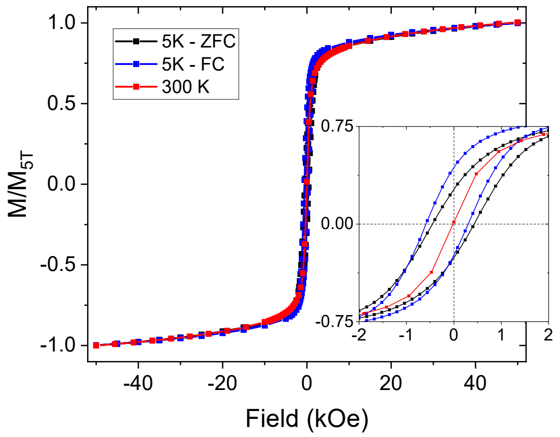

Figure S14. Normalized hysteresis loops at room temperature (300 K) and 5 K of pristine iron oxide nanoparticles (P1).

Comparison of the high field magnetic response of the samples

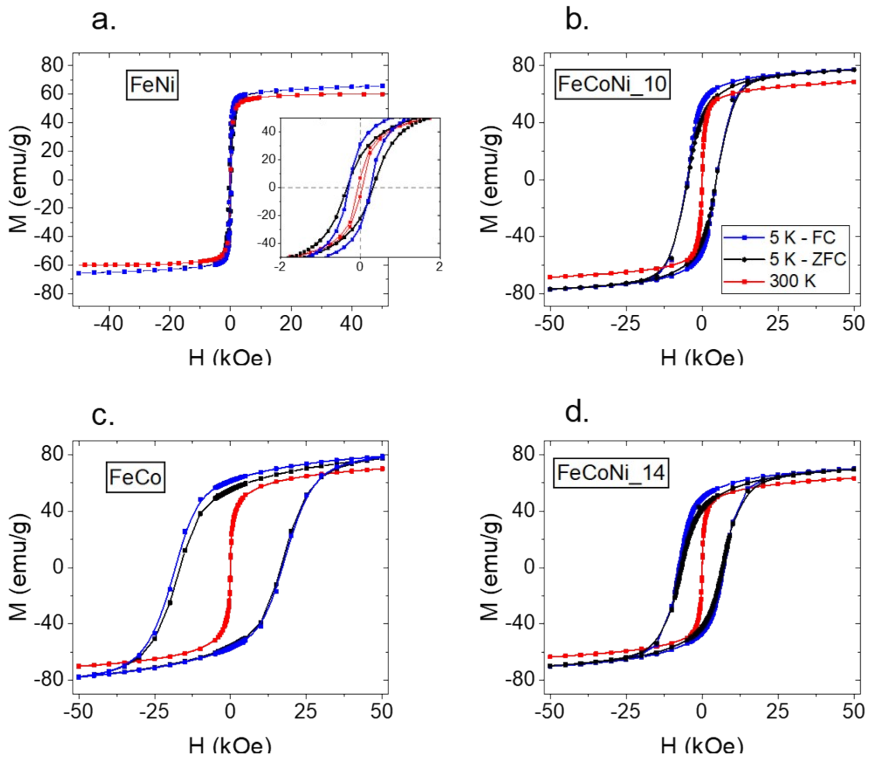

Figure S15. Hysteresis loops at different temperatures (5 K and 300 K), for all samples under study. 5 K loops are recorded after cooling in a zero field (ZFC) and under a 50 kOe magnetic field (FC). a) FeNi sample b) FeCoNi_10 c) FeCo and d) FeCoNi_14.

Figure S15 shows the ZFC and FC hysteresis loops at 5 K as well as the 300 K ones. The loop shift, the coercivity enhancement and the increase of the squareness (or reduced remanent magnetization, M_R/M_S), typical of exchange-biased systems, are clearly seen for all samples. Note that, for FeNi, although there is a change in the squareness parameter and in the reversal with the FC protocol (see inset in Figure S19a), there is a decrease in coercivity and a negligible exchange bias field with FC.

Estimation of interparticle dipolar energy

Dipolar energy or, alternatively, the temperature of dipolar energy, can be computed using the following relation:

$$T_{dd} = \frac{E_{dd}}{k_b} = \frac{\mu_0}{4\pi k_b} \frac{\mu^2}{<r>^3} = \frac{\mu_0}{4\pi k_b} \frac{(M_S V)^2}{<r>^3}.$$

Where k_b is the Boltzmann constant, μ_0 is the magnetic permeability of vacuum, V the volume of the nanoparticles, M_S the saturation magnetization and $<r>$ the average interparticle distance. As the nanoparticles were measured in powdered state but these powders were not pressed, it is safe to assume that the nanoparticles are separated by twice the length of the surfactant (oleic acid in this case), $2L_{OA}$. Thus, the center-to-center distance would be $2L_{OA} + d$, d being the nanoparticle diameter. It is noteworthy that this assumption is not overestimated since infrared spectra (Figure S5) do not revealed any contribution corresponding to free oleic acid molecules ($\nu_{C\text{-}O}$ = 1 700 cm^{-1}).

A comparison of T_{dd} and the apparent blocking temperature can be seen in Figure S16a, where it is clear that this energy represents a non-negligible contribution to the relaxation of the superspins. Yet, in Figure S16b, it is visible that the magnitude on the variations in TMAX are not solely due to dipolar interactions. In fact, they are mostly due to an increase in anisotropy. FeCoNi_14 is, however, an exception to this trend where the position of TMAX might be influenced in a sizable manner by dipolar interparticle interactions.

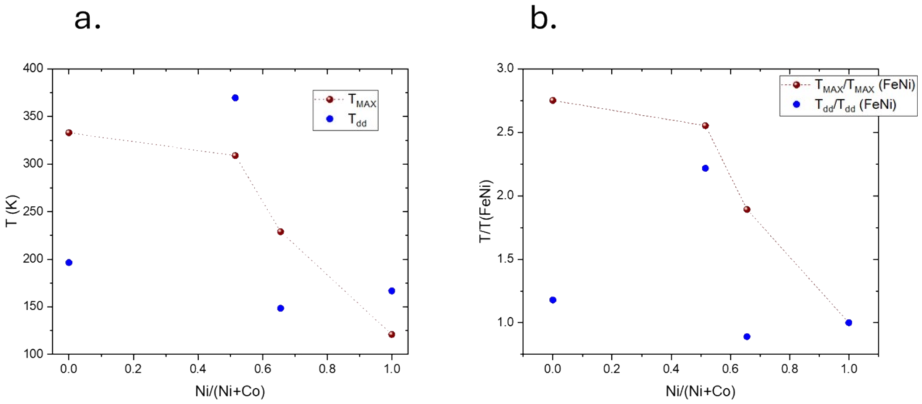

Figure S16. Comparison of dipolar energy (computed as T_{dd}) and T_{MAX} in a) absolute values and b) normalized to the values of FeNi sample.

Exchange bias and coercivity enhancement as a function of Ni/Co ratio

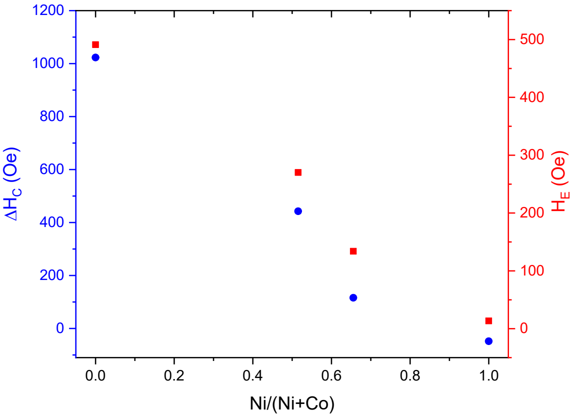

Figure S17. Coercivity enhancement and exchange bias field as a function of the Ni/(Ni+Co) ratio of the shell for all samples under study.